Effect of normal stress on the frictional behavior of brucite: Application to slow earthquakes at the subduction plate interface in the mantle wedge

Hanaya Okuda[1,2], Ikuo Katayama[3], Hiroshi Sakuma[4], Kenji Kawai[1]

[1]Department of Earth and Planetary Science, School of Science, University of Tokyo, Bunkyo, 113-0033 Tokyo, Japan

[2]Department of Ocean Floor Geoscience, Atmosphere and Ocean Research Institute, University of Tokyo, Kashiwa, 277-8564 Chiba, Japan

[3]Department of Earth and Planetary Systems Science, Hiroshima University, Higashi-Hiroshima, 739-8526 Hiroshima, Japan

[4]Research Center for Functional Materials, National Institute for Materials Science, Tsukuba, 305-0044 Ibaraki, Japan

Correspondence to: Hanaya Okuda (okuda@aori.u-tokyo.ac.jp)

Abstract

18   We report the results of friction experiments on brucite under both dry and wet conditions under

19   various normal stresses (10–60 MPa). The final friction coefficients of brucite were determined to be 0.40

20   and 0.26 for the dry and wet cases, respectively, independent of the normal stress. Under dry conditions,

21   velocity-weakening behavior was observed in all experiments at various normal stresses. Under wet

22   conditions, velocity weakening was observed at low normal stress (10 and 20 MPa), whereas velocity

23   strengthening was determined at a higher applied normal stress. Microstructural observations on recovered

24   experimental samples indicate localized deformation within a narrow shear band, implying that a small

25   volume of brucite can control the bulk frictional strength in an ultramafic setting. Among serpentinite-

26   related minerals, weak and unstable frictional behavior of brucite under the hydrated mantle wedge

27   conditions may play a role in slow earthquakes at the subduction plate interface in the mantle wedge.

1. Introduction

Serpentinite is generated by the hydration of ultramafic rocks and has various mineral compositions depending on temperature–pressure conditions of the $MgO–SiO_2–H_2O$ system (Evans et al., 2013). As serpentinite has been observed in various important tectonic settings and is considered to contribute to the weakness of serpentinite-dominant areas, the frictional properties of serpentinite have been investigated for several decades (see Guillot et al., 2015; Hirth and Guillot, 2013 for a review). A large volume of serpentinite is located in the mantle wedge in which olivine-rich rock of the upper mantle is hydrated by slab-derived water and composes the subduction plate interface as suggested by geological and seismological studies (Bostock et al., 2002; Christensen, 2004; Guillot and Hattori, 2013; Hyndman and Peacock, 2003; Kawahara et al., 2016; Kawakatsu and Watada, 2007; Mizukami et al., 2014; Peacock and Hyndman, 1999; Reynard, 2013). Because of the mechanical weakness of serpentinite, the relationship between the presence of serpentinite and the aseismic behavior below the downdip limit of seismogenic zones has been argued (Hyndman and Peacock, 2003; Oleskevich et al., 1999). However, many recent observations indicated that slow earthquakes, such as Episodic Tremor and Slip (ETS), Slow Slip Events (SSE), or Low-Frequency Earthquakes (LFE), occur at a depth of the mantle wedge in various subduction zones (Audet and Kim, 2016; Obara, 2002; Obara and Kato, 2016; Rogers and Dragert, 2003; Shelly et al., 2006). As those slow earthquakes can trigger or be triggered by huge megathrust earthquakes (Obara and Kato, 2016), the nucleation processes of slow earthquakes are important for understanding seismic activities at subduction zones.

Recent seismological and geological studies expect that several hundreds of meters to kilometers wide layer is serpentinized and foliated along the subduction plate interface, and the deformation of this serpentinite layer is likely to relate to slow earthquakes at a depth of the mantle wedge (Bostock et al., 2002; Calvert et al., 2020; DeShon and Schwartz, 2004; Dorbath et al., 2008; Kawakatsu and Watada, 2007; Nakajima et al., 2009; Ramachandran and Hyndman, 2012; Tarling et al., 2019). Within this foliated

54 serpentinite layer, both meta-ultramafic and meta-sedimentary blocks are present and metasomatic

55 reactions occur at the boundary between these blocks and the serpentinite matrix (Guillot et al., 2015;

56 Tarling et al., 2019). Such a block-in-matrix structure exhibits complex rheological behavior such that shear

57 stress is controlled by both ductile and brittle deformations of block and matrix depending on the strain rate

58 (Fagereng and den Hartog, 2017; den Hartog and Spiers, 2014; Niemeijer and Spiers, 2007; Tarling et al.,

59 2019). Thus, understanding the deformation properties of both block and matrix is essential to constrain

60 how the subduction plate interface behaves and generates slow earthquakes. This was also underlined by a

61 geological study on the Livingstone Fault, New Zealand (Tarling et al., 2019), which found that the

62 cataclastic slip surface was coated by scaly serpentinite, suggesting that the deformation process of

63 serpentinite is important for brittle deformation as well as widespread ductile deformation at the subduction

64 plate interface.

65   In addition, near lithostatic pore pressure conditions, which lead to low effective normal stress

66 conditions, have been inferred based on seismic velocity structures at the plate interfaces of several

67 subduction zones where slow earthquakes coincidently occur in the regions such as Cascadia, SW Japan,

68 Central Mexico, and Hikurangi (Audet et al., 2009; Audet and Kim, 2016; Eberhart-Phillips and Reyners,

69 2012; Matsubara et al., 2009; Shelly et al., 2006; Song and Kim, 2012). This low effective normal stress

70 condition may be correlated to slow earthquakes because frictional deformation becomes dominant, rather

71 than viscous deformation, in terms of shear strength (French and Condit, 2019; Gao and Wang, 2017).

72 Furthermore, the low effective normal stress condition seems favorable for the nucleation of slow

73 earthquakes (Liu and Rice, 2007, 2009; Rubin, 2008; Segall et al., 2010) and is also consistent with smaller

74 stress drops than regular earthquakes (Ide et al., 2007; Rubinstein et al., 2007, 2008; Schmidt and Gao,

75 2010). Thus, frictional properties of serpentinite under the low effective normal stress condition likely play

76 an important role in slow earthquakes at the subduction plate interface near the mantle wedge.

77   Serpentinite in the mantle wedge is mainly composed of an antigorite–olivine assemblage in

78 warm subduction zones like Cascadia, whereas a brucite–antigorite assemblage dominates in the case of

79 cold subduction zones such as that in NE Japan (Peacock and Hyndman, 1999). Because fluids from

80 subducting slabs have a high SiO_2 content, talc is stable in the vicinity of the slab–mantle boundaries

81 (Hirauchi et al., 2013; Peacock and Hyndman, 1999). Serpentinite is made up of serpentinite-related

82 minerals, such as antigorite, brucite, and talc, and as those minerals show different frictional behavior, the

83 frictional properties of each mineral should be understood to interpret the mechanical behavior of bulk

84 serpentinite. Many previous experimental studies investigated the frictional properties of antigorite and talc

85 (Hirauchi et al., 2013; Moore et al., 1997; Moore and Lockner, 2007, 2008; Okazaki and Katayama, 2015;

86 Reinen et al., 1994; Sánchez-Roa et al., 2017; Takahashi et al., 2007; Tesei et al., 2018). However, brucite

87 has rarely been considered in previous studies, as it is challenging to detect brucite under natural conditions

88 because of its fine-grained nature (Hostetler et al., 1966). Brucite is not thermodynamically stable when the

89 slab-derived water contains high SiO_2 content, and the mantle wedge may undergo the silica metamorphism

90 (Manning, 1997; Peacock and Hyndman, 1999). However, geological works on the exhumed mantle wedge

91 regions suggested that the silica metamorphism has not occurred widely within the shallow mantle wedge

92 because talc zones or metasomatic reactions are often limited in the narrow part near the meta-sedimentary

93 rocks (Angiboust and Agard, 2010; D'Antonio and Kristensen, 2004; French and Condit, 2019; Guillot et

94 al., 2009; Kawahara et al., 2016; Mizukami et al., 2014; Nagaya et al., 2020; Reynard, 2013; Tarling et al.,

95 2019). These observations indicate that the serpentinite layer at the subduction plate interface may contain

96 brucite because of low silica metamorphism as brucite itself has sometimes been found (Kawahara et al.,

97 2016; Mizukami et al., 2014). Hydrothermal experiments also support the finding that the SiO_2 is effectively

98 consumed and brucite can stably exist with antigorite (Oyanagi et al., 2015, 2020). Although deformation

99 may localize at the metasomatic region (Hirauchi et al., 2013; Tarling et al., 2019), the foliated structure of

100 serpentinite matrix implies that the serpentinite layer still accompanies some portion of deformation at the

101 subduction plate interface. Furthermore, as brucite is a sheet-structure mineral, which often shows a low

102 friction coefficient due to weak interlayer bonding, its frictional behaviors may play a role in earthquakes

103 at the serpentinite layer (Moore et al., 2001; Moore and Lockner, 2004).

104   Only a few previous experimental studies under high normal stress conditions of 100 or 150 MPa

105 have been conducted on the frictional properties of brucite. It was shown that brucite has friction

106 coefficients of 0.40–0.46 (dry) or 0.28 (wet), which are lower than those of antigorite (Moore and Lockner,

107 2004, 2007; Morrow et al., 2000). Regarding the velocity dependence, significant stick-slip behavior has

108 been observed for dry brucite at both room and high temperature, implying velocity-weakening behavior.

109 Conversely, wet brucite shows velocity-strengthening behavior at room temperature, which gradually

110 changes to velocity weakening with increasing temperature (Moore et al., 2001; Moore and Lockner, 2007).

111 The friction coefficient of a serpentinite gouge can be lowered by approximately ~10–15 % due to the

112 presence of brucite (Moore et al., 2001). The weakness and velocity-weakening behavior of brucite under

113 certain conditions might affect nucleation processes of slow earthquakes at the subduction plate interface

114 in the mantle wedges because velocity-weakening behavior is likely to relate to slow earthquakes as

115 proposed in previous studies. The dilatancy hardening in the velocity-weakening system (Rubin, 2008;

116 Segall et al., 2010), the slip-weakening (Ikari et al., 2013), the transition from the velocity-weakening to

117 velocity-strengthening system at a cut-off velocity (den Hartog et al., 2012; Matsuzawa et al., 2010;

118 Shibazaki and Iio, 2003), or the slow stick-slip (Leeman et al., 2016, 2018; Okazaki and Katayama, 2015)

119 are proposed as mechanisms that generate slow earthquakes. Most of them require the velocity-weakening

120 system to nucleate earthquakes, especially for seismologically detected events like LFEs; therefore, the

121 velocity-weakening behavior of brucite can be suggestive of slow earthquakes at the subduction plate

122 interface.

123   However, the frictional behavior of brucite at low effective normal stress has not been studied in

124 spite of its potential relationship to slow earthquakes. In this study, we experimentally investigated the

125 frictional behavior of brucite at various effective normal stresses ranging from 10 to 60 MPa to understand

126 the effect of brucite on the seismic activities at the subduction plate interface in hydrated mantle wedges.

127

2. Methods

2.1. Friction experiment

2.1.1. Sample preparation

131 Brucite nanoparticles with a grain size of 70 nm chemically synthesized by FUJIFILM Wako

132 Pure Chemical Corporation were used for the friction experiments to simulate its fine-grained nature (Fig.

133 1). The synthetic samples had a purity of 99.9 % (data from FUJIFILM Wako Pure Chemical Corporation).

134 A biaxial testing machine at Hiroshima University, Japan, was used for all friction experiments

135 in this study (Noda and Shimamoto, 2009). There are two gouge layers between three gabbro blocks (Fig.

136 1). The surfaces in contact with gouges were roughened before the experiments using Carborundum (grit

137 80) to prevent slip between the blocks and sample. All brucite samples were dried in the vacuum oven

138 overnight under 120 °C before the experiments. This temperature was selected to remove adsorbed water

139 and prevent the dehydroxylation of brucite into periclase (MgO). For the dry experiments, the brucite

140 powder was quickly sandwiched between the blocks to form the gouge after removing it from the vacuum

141 oven, and the blocks with samples were then put in the testing machine. For the wet experiments, dried

142 brucite was mixed with distilled water before placing it in the gouges and then sandwiched between blocks.

143

2.1.2. Experimental procedures

145 Normal stress was horizontally applied on the side blocks, and shear stress was applied vertically

146 by pushing the center block downward (Fig. 1). Before applying shear stress, the desired normal stress was

147   applied to the blocks for 1 h to prevent an effect of the compaction of the gouge during shear deformation

148   (nominally precompaction). For the wet experiments, the blocks and gouges were placed in the tank filled

149   with distilled water for 1 h under a normal stress of 250 kPa before the precompaction with the desired

150   normal stress such that water-wet conditions were achieved. Note that as we did not have any mechanism

151   to prevent the gouge from squeezing out for the wet experiment; therefore, the gouge thickness for wet

152   experiments becomes narrower than that for dry ones. After the precompaction, shear stress was applied

153   with a constant load point velocity of 3 μm s^{-1}. Velocity step tests were repeatedly conducted after the shear

154   displacement reached 10 mm by abruptly increasing the load point velocity to 33 μm s^{-1} and decreasing it

155   to 3 μm s^{-1} after a shear displacement of 1 mm (Fig. 2). The normal stress conditions of 10, 20, 40, and 60

156   MPa were tested for both the dry and wet cases to study the influence of effective normal stress. In addition,

157   several experiments were conducted with different total shear displacements to investigate the evolution of

158   the gouge microstructure in both the dry and wet experiments (Table 1).

159

160
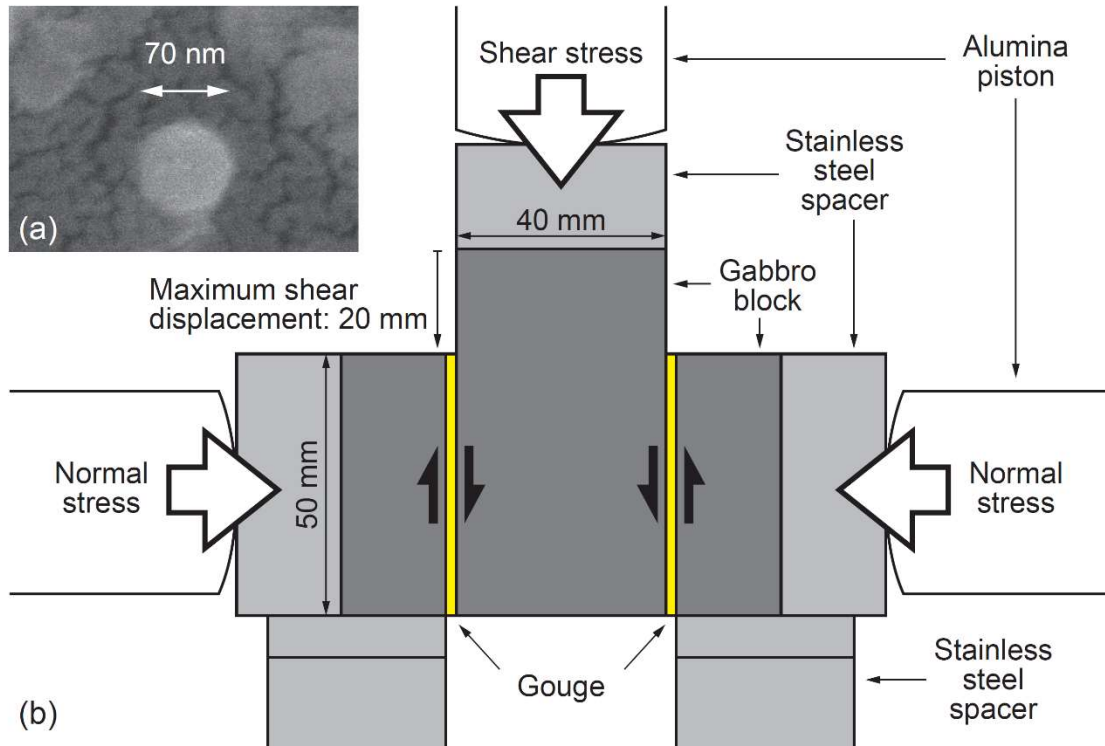
161 **Figure 1: (a) SEM micrograph of synthetic brucite used in this study. (b) Schematic view of the biaxial testing**
162 **machine used in this study.**

163

164

165 **2.2. Data analysis**

166 **2.2.1. Mechanical data**

167   The friction coefficient μ was calculated from the ratio of the shear stress to the normal stress.

168 Note that cohesion stresses were 0.36 and 0.47 MPa for dry and wet cases, respectively, calculated by linear

169 regression of shear stress and normal stress of all the experiments. Because the obtained cohesion stresses

170 were too small to affect the friction coefficients, the cohesion stress was not considered in this study. The

171 shear displacement was corrected using the stiffness of the testing machine (4.4×10^8 N m^{-1}). The velocity

172 step tests were analyzed using the rate- and state-dependent friction (RSF) law (Dieterich, 1979; Ruina,

173 1983). Before conducting the following analyses, the friction coefficient versus the displacement curve was

174 detrended for the slip-weakening trend, which was obtained from the friction data in the second half of each

175 velocity step of 500 μm shear displacement. Detrended data were fitted to the following the RSF law:

176 $$\mu = \mu_0 + a \ln\left(\frac{V}{V_0}\right) + b_1 \ln\left(\frac{V_0 \theta_1}{d_{c1}}\right) + b_2 \ln\left(\frac{V_0 \theta_2}{d_{c2}}\right), \tag{1}$$

177 where a, b_1 and b_2 are nondimensional parameters, μ_0 is the steady-state friction coefficient before the

178 velocity step, V_0 and V are the sliding velocities before and after the velocity step, d_{c1} and d_{c2} are the

179 characteristic slip distances, and θ_1 and θ_2 are the state variables. We estimated the effect of elastic

180 interaction due to the machine stiffness on V using the following relationship:

181 $$\frac{d\mu}{dt} = k\left(V_{lp} - V\right), \tag{2}$$

182   where V_{lp} is the load point velocity, which was abruptly changed, and k is the system stiffness, which was

183   treated as an unknown parameter (in μm^{-1}). The Dieterich (aging) law (Dieterich, 1979; Marone, 1998;

184   Ruina, 1983) was used for the state variable in this study.

185
$$\frac{d\theta_i}{dt} = 1 - \frac{V\theta_i}{d_{ci}}, i = 1, 2 \tag{3}$$

186   A MATLAB code, RSFit3000, developed to fit the velocity step and slide hold slide tests (Skarbek and

187   Savage, 2019) was used for the analyses of velocity step tests. Second variables b_2, θ_2, and d_{c2} (Blanpied

188   et al., 1998) were only introduced when the experimental data were poorly fitted (upsteps of HTB575 and

189   HTB598; Fig. 4); otherwise, b_2 and θ_2 were treated as 0. The value of $a - b$ ($a - b_1 - b_2$, or $a - b_1$)

190   was then calculated for each step, which describes the instability of the simulated fault: the state of fault is

191   defined as velocity strengthening and stable when $a - b$ is positive, whereas it is defined as velocity

192   weakening and potentially unstable when $a - b$ is negative. Note that d_c values for the velocity steps

193   whose velocities decreased from 33 to 3 μm s^{-1} (downsteps) are larger than those for the velocity steps

194   whose velocities increased from 3 to 33 μm s^{-1} (upsteps). Because we chose to use the Dieterich (aging)

195   law to fit the RSF law, d_c reflects the diameter of the contact area between grains (Dieterich, 1979; Ruina,

196   1983). When the load point velocity is 3 μm s^{-1}, the lifetime of one contact area is longer than that with a

197   load point velocity of 33 μm s^{-1}. Therefore, the contact diameter, d_c, for the load point velocity of 3 μm

198   sec^{-1} (downsteps) is larger than that for 33 μm s^{-1} (upsteps). In addition, d_c is also considered to reflect the

199   shear localization (Marone and Kilgore, 1993); when the shear localizes, d_c decreases. Hence, the

200   difference in d_c has qualitative information on the shear localization within the gouge. Although there are

201   still debates on the choice of constitutive laws (Bhattacharya et al., 2015, 2017; Marone, 1998), as all

202   constitutive laws give the same result on $a - b$, we calculated the value of $a - b$ by using separately

203   obtained a and b with the aging law. The focus of this study will be the $a - b$ value because it plays an

204   essential role in the nucleation process of earthquakes. However, other parameters like d_c and stiffness are

205   also important to the nucleation process, and therefore, those parameters should be assessed in future studies.

206 When the system is velocity weakening, that is, $a - b$ is negative, it starts to vibrate

207 automatically (stick-slip) when the system stiffness is lower than a critical stiffness, whereas conditionally

208 stable sliding is achieved when the system stiffness is higher than a critical stiffness. The critical stiffness

209 k_c can be described as follows when quasi-static stick-slip behavior is assumed:

210
$$k_c = \frac{N(b - a)}{d_c}, \tag{4}$$

211 where N is the effective normal stress (Ruina, 1983). Thus, as the effective normal stress N applied to the

212 velocity-weakening system increases, the system starts to show stick-slip behavior. In other words, the

213 occurrence of stick-slip represents that the system is velocity-weakening. We determined the $a - b$ value

214 for dry experiments with normal stresses of 40 and 60 MPa by simply comparing the averaged friction

215 coefficients during the stick-slip behavior for two velocities based on the following relationship:

216
$$a - b = \frac{\Delta \mu_{ss}}{\Delta \ln V}, \tag{5}$$

217 where $\Delta \mu_{ss}$ and $\Delta \ln V$ are variations in the steady-state friction coefficient and the sliding velocity in the

218 log scale, respectively. In this case, neither a, b, nor d_c can be determined.

219

220 **2.2.2. Microstructure**

221 In the case of sheet-structure minerals, the friction between basal planes of the crystals [(0001)

222 plane for brucite] is thought to be significant due to their weak bonding. The shear surfaces of the samples

223 recovered from friction experiments using sheet-structure minerals often show smooth surfaces composed

224 of platy particles aligned parallel to the sliding direction (Moore and Lockner, 2004). Further, according to

225 the experiments with natural samples, the aligned platy particles of interconnected talc were reported to

226 contribute to the low friction coefficient of low angle normal faults (Collettini et al., 2009).

227 Because these experiments indicate that the crystal orientation within the gouge has a significant

228 effect on the friction coefficients of sheet-structure minerals, observations of thin sections of recovered

229   samples were conducted after the experiments (Table 1) to investigate the effects of the deformation

230   structures and crystal orientation within the gouges on the frictional behavior. After the experiment, we

231   impregnated the gouge and the blocks with epoxy resin to keep the deformation structures within the gouge.

232   Thin sections parallel to the shear direction and normal to the gouges with a thickness of 30 μm were

233   prepared from the impregnated samples. The scanning electron microscope (SEM, JEOL JXA-8900 at the

234   Atmosphere and Ocean Research Institute, University of Tokyo, Japan) was used to observe the

235   microstructures of the gouges. An accelerating voltage of 15 kV and a beam current of 10.0 nA were used

236   for all backscattered electron (BSE) observations. The crystal orientation was determined with a polarizing

237   microscope at the University of Tokyo, Japan.

238

239   **3. Results**

240   **3.1. Mechanical behaviors**

241   **3.1.1. Friction coefficients**

242   In general, both dry and wet experiments show high friction coefficients at a shear displacement

243   of 1.5–2 mm (hereafter peak friction coefficients) followed by slip-weakening trends with a shear

244   displacement of about 10 mm towards steady state (Figs. 2 and S1). The final friction coefficients at a shear

245   displacement of ~20 mm for dry and wet conditions under all normal stress conditions were 0.40±0.04 and

246   0.26±0.03, respectively (Table 1). These final friction coefficients are mostly independent of the applied

247   normal stress (Fig. 3) and consistent with previous experimental results, that is, 0.38-0.46 and 0.28 for dry

248   and wet brucite at an applied normal stress of 100 MPa at room temperature, respectively (Moore and

249   Lockner, 2004, 2007). The friction coefficient for dry experiments is also close to the theoretical value of

250   0.30±0.03 (Okuda et al., 2019). Note that the peak friction coefficient of wet brucite at an effective normal

251   stress of 60 MPa is high because of sudden stress drops in the initial stage of the shear displacement (Fig.

252 S1). As this data may include some experimental artifacts, we do not use this peak value for 60 MPa normal

253 stress in this study.

254

255

256
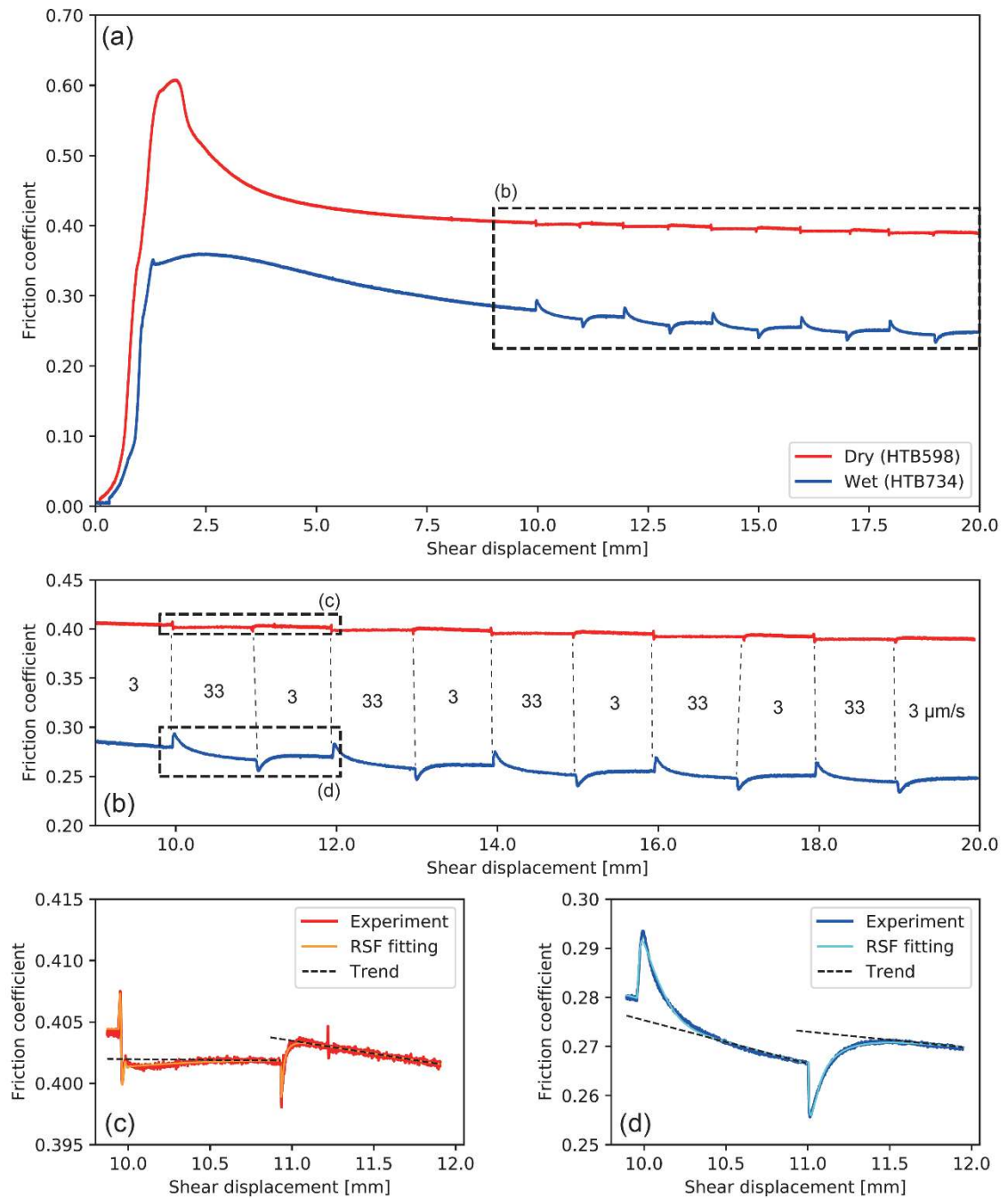
257 **Figure 2: (a) Friction coefficients for dry (HTB598) and wet (HTB734) experiments at a normal stress of 20 MPa.**

258 **Slip-weakening behavior was observed after the peak under both dry and wet conditions. (b) Enhanced view of**

259 **velocity step sequences as indicated by the dotted square in (a). The velocities at given shear displacements are**

260 **displayed between two lines. (c & d) Enhanced views of velocity steps in the squares in (b). Second variables**

261 **were introduced for upsteps of HTB598 (c).**

262

263
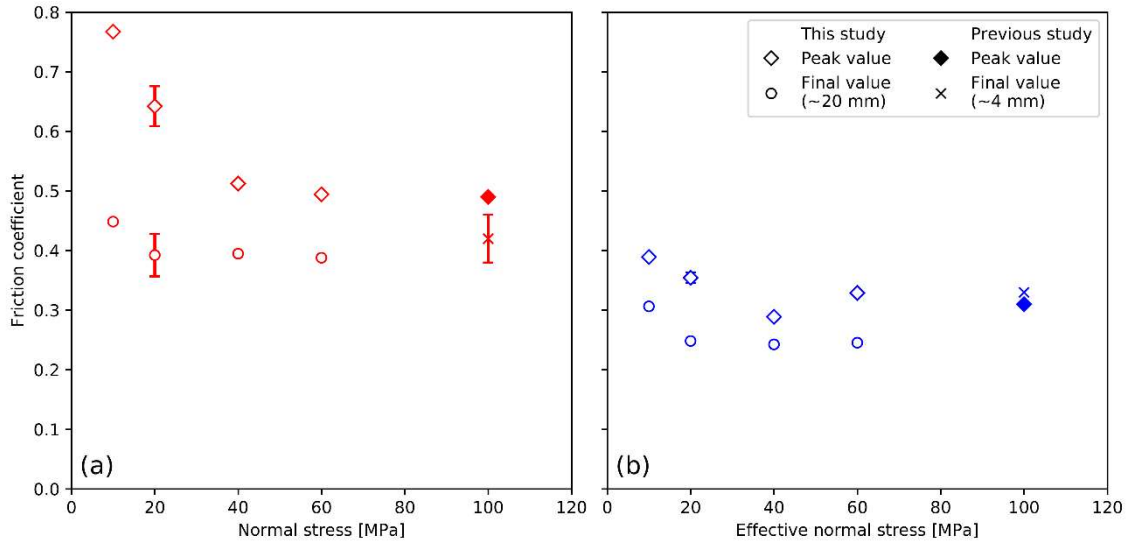
264 **Figure 3: Relationship between normal stress and the peak or final friction coefficients for the dry (a) and wet**

265 **(b) experiments. Data at a normal stress of 100 MPa were obtained from previous experiments (Moore et al.,**

266 **2001; Moore and Lockner, 2004, 2007; Morrow et al., 2000). The final friction coefficients do not show a clear**

267 **trend with normal stress. For this study, the error bar represents the one-sigma standard deviation among**

268 **multiple data. For 100 MPa dry data, the final friction coefficient and the error bar denote the averaged value**

269 **of stick-slip behavior and its amplitude, respectively. Note that the peak friction coefficient of wet brucite at an**

270 **effective normal stress of 60 MPa is high because of sudden stress drops in the initial stage of the shear**

271 **displacement (Fig. S1). As this data may include some experimental artifacts, we do not use this peak value in**

272 **this study.**

273

274 **3.1.2. Velocity dependencies**

275   For wet experiments, negative $a - b$ values were observed at low normal stresses of 10 and 20

276 MPa (Figs. 4a and b). However, the $a - b$ values became almost neutral at 40 MPa and positive at 60 MPa.

277 A positive $a - b$ value was consistent with the previous experiments on wet brucite at an effective normal

278   stress of 100 MPa (Moore et al., 2001; Moore and Lockner, 2007). The $a - b$ values obtained for the

279   upsteps and downsteps insignificantly differ (Figs. 4a and b). In the experiments with normal stress

280   conditions of 20, 40, and 60 MPa, the constitutive parameter a is almost constant with 0.0054 for both

281   upsteps and downsteps, whereas b decreases from 0.0064 to 0.0042 and from 0.0076 to 0.0040 for upsteps

282   and downsteps, respectively, as the normal stress increases (Figs. 4e and f). Accordingly, we concluded

283   that the decrease in b induces the transition from negative to positive $a - b$. The d_c values at different

284   effective normal stresses insignificantly differ (Figs. 4c and d).

285   For dry experiments, negative $a - b$ values were obtained at all normal stress conditions (Figs.

286   4a and b). When the normal stress was higher than 40 MPa, stick-slip behavior was observed. This unstable

287   stick-slip behavior was also reported in the case of the dry experiment at a higher normal stress of 100 MPa

288   (Moore and Lockner, 2004; Morrow et al., 2000). No information on a, b, and d_c values for 40 and 60

289   MPa experiments was obtained because of the stick-slip behavior. As shown in the wet conditions, larger

290   d_c values were observed for the downsteps (Figs. 4c and d). Note that the second variables b_2 and d_{c2}

291   were introduced in two experiments (HTB575 and HTB598). However, their effects on the earthquake

292   nucleation process, that is, $a - b$ value, are small because the b_2 values are much smaller than b_1,

293   although d_{c2} value is much larger than d_{c1} (Fig. 4e and Table S1).

294   The constitutive parameters a and b and critical slip distance d_c of the dry and wet

295   experiments significantly differ. The a, b, and d_c values of the wet experiments are larger than those of

296   the dry experiments (Fig. 4). The critical slip distances d_c of the upsteps and downsteps under wet

297   conditions were 5–15 times and 3–4 times larger than those under dry conditions, respectively.

298

299

300
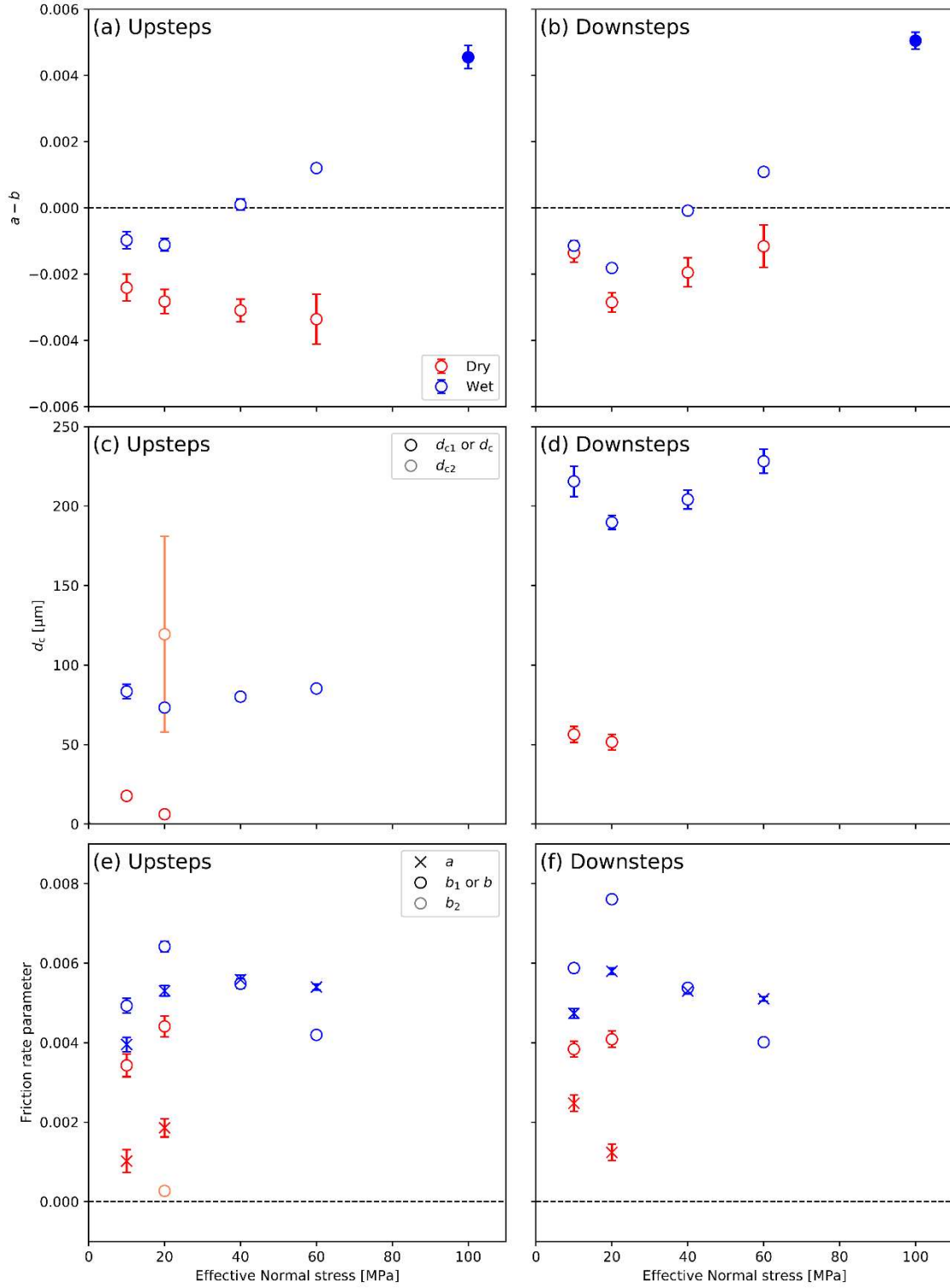
301 **Figure 4: Results of the velocity step tests. Values of $a - b$ for upsteps (a) and downsteps (b), d_c for upsteps**

302 **(c), and downsteps (d), a and b for upsteps (e), and downsteps (f). The errors represent the one-sigma standard**

303 **deviations of all upsteps or downsteps under each experimental condition, including the errors of the nonlinear**

304 **least-square fitting processes. The $a - b$ values at a normal stress of 100 MPa were obtained from a previous**

305 **study (solid symbol; Moore et al., 2001). Because stick-slip behavior was observed in the dry experiments at**

306 **normal stresses of 40 and 60 MPa, $a - b$ values were calculated by eq. 5 (Sect. 2.2.1). Second variables b_2 and**

307 **d_{c2} were introduced for upsteps of the dry experiments at a normal stress of 20 MPa.**

308

3.2. Microstructure

3.2.1. Evolution of deformation structures

311 As all samples (both dry and wet) showed a peak value followed by a transition into the steady

312 state, we chose shear displacements before the peak friction coefficient (pre-yield), after the peak friction

313 coefficient (post-yield), and in the steady state (10 mm) to study the evolution of the deformation structures.

314 Note that the steady state may not be achieved at a shear displacement of 10 mm, but as the final friction

315 coefficients were similar to the friction coefficients at 10 mm shear displacement, here we used the term

316 "steady state" and considered that the microstructure at 10 mm shear displacement might be consistent with

317 the steady state. We followed the description of the microstructure of a sheared gouge by Logan et al.

318 (1979). The results for the dry and wet experiments are shown in Figs. 5 and 6, respectively.

319 Before the shear loading, no shear structure was observed (Fig. 5a). When the shear force was

320 loaded, the Riedel shear propagated in the pre-yield regime, and the gouge thickness decreased rapidly at

321 first (Figs. 5b and 6a). Subsequently, the boundary shear started to develop in the post-yield (Figs. 5c and

322 6b). In the steady state, the boundary shear was created, and the Riedel shear tilted subparallel to the

323 boundary shear (Figs. 5d and 6c). The surfaces of the gabbro blocks were filled with brucite, and the

324 boundary shear was much smoother than the original block surface. These observations are consistent with

325 previous studies (Haines et al., 2013; Kenigsberg et al., 2019, 2020; Logan et al., 1992; Marone, 1998),

326 although clear Y shear and P foliation were not observed in this study. The gouge thickness remained almost

327 constant after the post-yield and steady state, suggesting that the deformation may localize parallel to the

328 shear deformation, i.e., parallel to the boundary shear. The thickness of the entire gouge in the steady state

329 was 400 and 150 μm in the dry and wet cases, respectively (Figs. 5d and 6c). The narrow thickness of the

gouge in the wet case may result from the leakage of the sample during the experiment, but we did not have

any mechanism to prevent the gouge from leaking out. The difference in the entire gouge thickness may

not affect the overall frictional characteristics because both dry and wet cases showed the Riedel shear

development at first, followed by the boundary shear development. Observation of grain contact is needed

for clarification, but it was not possible in this study because the grains were very small (70 nm in diameter).
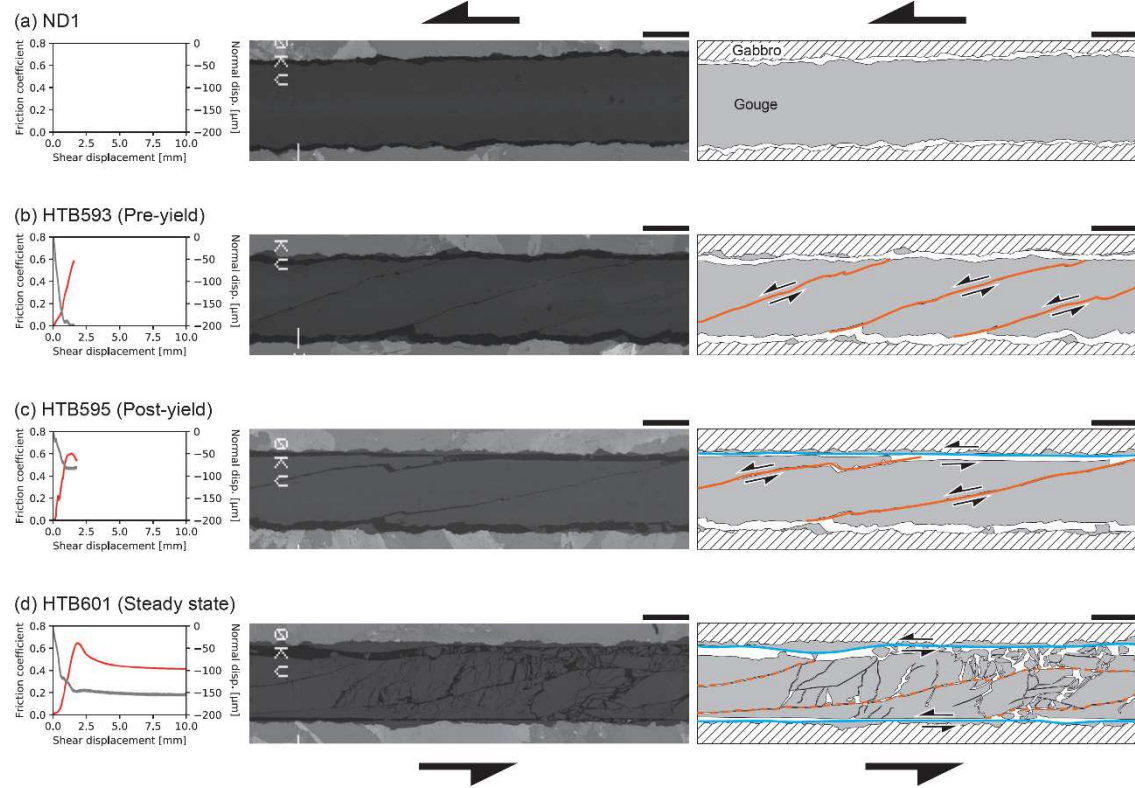
Figure 5: Backscattered electron (BSE) images showing the deformation of gouges (center) and corresponding interpretive sketches (right) of the dry experiments. The friction coefficients and normal displacement are shown in the left panels using colored and gray lines. The orange lines, blue lines, gray area, hatched area, and white area in the sketches correspond to the Riedel shear, boundary shear, brucite gouge, gabbro block, and epoxy resin, respectively. The orange dot lines are the Riedel shears, which may not be active. The arrows represent the slip directions. The scale bars represent 200 μm.

344
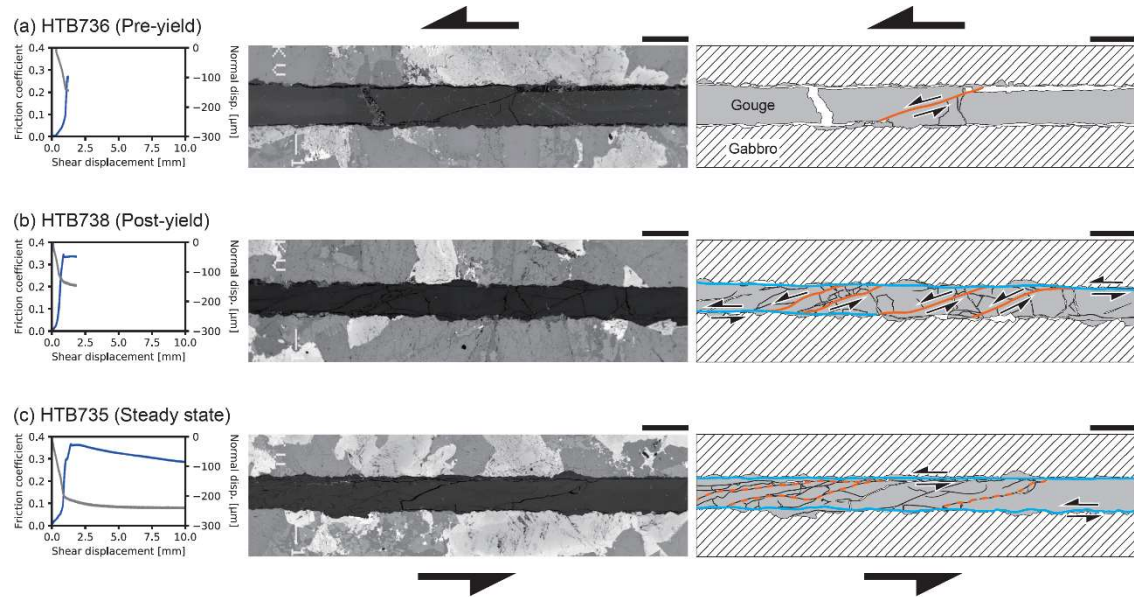
345 **Figure 6: Backscattered electron (BSE) images showing the deformation of gouges (center) and corresponding**

346 **interpretive sketches (right) of the wet experiments. See Fig. 5 for descriptions.**

347

348 **3.2.2. Crystal orientation**

349   Because brucite has a negative elongation (Berman, 1932) and its birefringence is 0.014–0.020

350 (Deer et al., 2013), the interference color of brucite under crossed nicols with the sensitive color plate

351 inserted becomes second-order blue or first-order yellow when the c axis of brucite is normal or parallel to

352 the X′-direction of the sensitive color plate, respectively.

353   In the dry sample (HTB601; Figs. 7a and 7b), a second-order blue line can be observed parallel

354 to the smooth boundary shear, implying that the basal (0001) plane of the brucite particles is aligned along

355 the boundary shear parallel to the shear direction. We did not observe any alignment along the Riedel shears,

356 suggesting that deformation along the Riedel shears cannot be dominant at the steady state. Based on the

357 magnified view, the brucite particles are oriented within 10 μm around the boundary shear (Fig. 7b).

358 Because the purple area indicates that the brucite particles are randomly oriented, the shear strain can be

359 localized within a thickness of 10 μm. Hereafter, we call this oriented area "shear band." In the wet samples,

360 the crystals are also oriented along the boundary shear (Figs. 7c and 7d). The thickness of the shear band is

361 20 µm (Fig. 7d), which is a little wider than that for the dry experiments. This observation is consistent with

362 the relationship between the shear localization and d_c value (Marone and Kilgore, 1993): the degree of

363 shear localization for the dry sample is higher than that for the wet sample, and d_c for dry sample was

364 smaller than for wet sample (Fig. 4). Note that detailed transmission electron microscopy is required in

365 future studies to confirm the crystal orientation and shear band thickness, as shown in previous studies

366 (Verberne et al., 2014a; Viti, 2011).

367

368
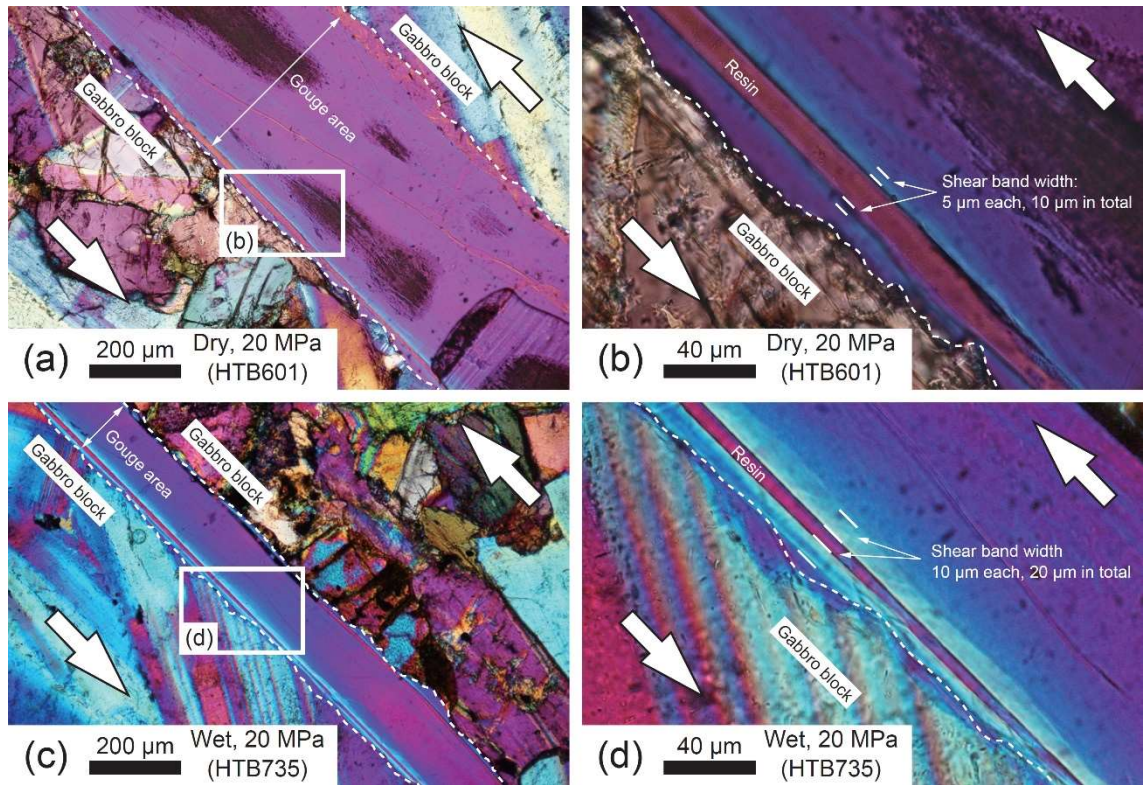
369 **Figure 7: Observation of the crystal orientation using the polarizing microscope under crossed nicols with the**

370 **sensitive color plate. The arrows indicate the shear direction. The X′-direction of the sensitive color plate is**

371 **parallel to the shear direction. (a) Dry experiment with 20 MPa normal stress (HTB601). (c) Wet experiment**

372 **with 20 MPa normal stress (HTB735). (b and d) Magnified views of (a) and (c), respectively. The shear band**

373 **thicknesses are indicated in the figures. The white dashed line represents the boundary between the gabbro**

374 **block and the brucite gouge.**

375

4. Discussion

4.1. Mechanical weakness of a small amount of brucite

Based on the microstructural observations in Sect. 3.2, the boundary shear is smooth, filling the rough surface of the gabbro block as a "fault mirror" (Siman-Tov et al., 2013). The brucite particles are aligned along the boundary shear, suggesting that the deformation within the narrow shear band is responsible for most of the deformation of the gouge during the steady state. In addition, the constant gouge thickness during the steady state suggests that the gouge deformation occurs parallel to the shear direction, consistent with shear deformation localized within the shear band.

Because previous studies showed that a smooth slip surface reduces the friction coefficient compared to a roughened slip surface (Anthony and Marone, 2005), the development of the smooth boundary shear observed in this study would reduce the friction coefficient with increasing shear displacement (Haines et al., 2013). In addition, the slip between the basal planes of sheet-structure minerals also plays an important role for weak friction because the friction between single crystals of sheet-structure minerals has a lower friction coefficient than that of powdered samples (Horn and Deere, 1962; Kawai et al., 2015; Niemeijer, 2018; Okamoto et al., 2019). Based on the observed alignment of the basal plane of brucite within the shear band, the friction between the basal planes of brucite crystals might enhance the weak friction of brucite. Because the preferred planes of nanoparticles tend to be aligned even when the velocity is low (Verberne et al., 2013, 2014b), nanoparticles could contribute to the slip-weakening behavior. Based on these phenomena, we conclude that the mechanical weakness of brucite observed in this study is likely derived from the smooth boundary shear of fine brucite particles and alignment of the basal plane of brucite parallel to the boundary shear.

The results of several previous experimental studies showed that the friction coefficient of a mixture of strong and weak materials inversely correlates with the volume of the weak materials (Giorgetti et al., 2015; Logan and Rauenzahn, 1987; Moore and Lockner, 2011; Niemeijer and Spiers, 2007;

400 Shimamoto and Logan, 1981; Takahashi et al., 2007; Tembe et al., 2010). Based on the maximum amount

401 of brucite in serpentinite, that is ~20 vol. % (Kawahara et al., 2016; Moore et al., 2001), the expected

402 friction coefficient of the antigorite–brucite mixture is 0.53, assuming a simple linear mixing law between

403 the wet friction coefficients of 0.6 for antigorite and 0.26 for brucite. This value is not small, but the bulk

404 friction coefficient of the mixture will decrease if weak brucite crystals are interconnected with each other.

405 The microstructural observations showed that the shear band is less than 50 μm wide (Sect. 3.2.2; Fig. 7);

406 therefore, a narrow network of brucite can decrease the bulk strength. The results of a recent petrographic

407 study of a hydrated paleo-mantle wedge revealed brucite thin films parallel to antigorite particles,

408 suggesting the significant role of brucite in the development of the sheared structure of the antigorite–

409 brucite assemblage in the hydrated mantle wedge (Mizukami et al., 2014). Because the maximum thickness

410 of the brucite film in the antigorite–brucite assemblage is several hundred micrometers (Kawahara et al.,

411 2016; Mizukami et al., 2014), that is, larger than 50 μm, brucite has the potential to weaken the bulk strength

412 of serpentinite drastically.

413

414 **4.2. Application to the mantle wedge conditions**

415   When we consider the effect of brucite on the seismic activities in the mantle wedge, the effect

416 of temperature should be taken into account because all our experiments were conducted under room-

417 temperature conditions. According to previous experiments on brucite under hydrothermal conditions in

418 which the temperature was varied, the friction coefficient and the $a - b$ values decrease with increasing

419 temperature (Moore et al., 2001; Moore and Lockner, 2007). Because a nearly neutral $a - b$ value was

420 observed at an effective normal stress of 150 MPa and a temperature of 340 ℃ (Moore et al., 2001), brucite

421 shows unstable behavior under a wide range of temperature–pressure conditions, especially at low effective

422 normal stress. Based on the estimated frictional properties of brucite under the mantle wedge condition, we

423 compared brucite to other mineral phases to interpret the earthquake processes within the mantle wedge

424 (Fig. 8).

425   In the mantle wedge, ultramafic minerals, such as olivine, transform into serpentine minerals,

426 such as antigorite, talc, and brucite, due to hydration. In cold subduction zones, such as beneath NE Japan,

427 likely containing brucite under the temperature–pressure conditions of the mantle wedge, the

428 thermodynamically stable mineral assemblages are lizardite-brucite (Liz–Brc) at depths shallower than 50

429 km or antigorite–brucite (Atg–Brc) assemblage under deeper and warmer conditions (Peacock and

430 Hyndman, 1999). Previous experimental studies on antigorite suggested potential seismic activities due to

431 the unstable frictional behavior of antigorite at high temperatures above 450 ℃ (Okazaki and Katayama,

432 2015; Takahashi et al., 2011) at which crustal (granitic) rock shows stable friction (Fig. 8), whose friction

433 coefficient (0.5–0.7) is not as low as that of brucite (Fig. 8). Although lizardite, which thermodynamically

434 destabilizes at ~200 ℃, potentially shows unstable frictional behavior at low temperature (Moore et al.,

435 1997), its friction coefficient is 0.4–0.5, lower than that of antigorite but higher than that of brucite (Fig. 8).

436 Therefore, antigorite and lizardite are not preferably deformed if other weaker minerals, such as brucite,

437 are present in continuous fault strands in which the deformation localizes.

438   Another candidate for such a weak mineral stable under mantle wedge conditions is talc. Talc

439 has a low friction coefficient of 0.1–0.2 at low to high temperatures (Fig. 8); therefore, it might contribute

440 to the creep behavior of the San Andreas fault (Moore and Lockner, 2008) or weaken the slab–mantle

441 interface (Hirauchi et al., 2013; Hyndman and Peacock, 2003). However, because talc has a stable frictional

442 behavior at any temperature, leading to aseismic creep (Moore and Lockner, 2008; Sánchez-Roa et al.,

443 2017), it cannot nucleate earthquakes. When we consider talc in the mantle wedge, talc is

444 thermodynamically stable at high Si concentrations and temperature. Whereas, the mineral assemblage

445 consists of brucite and antigorite when the Si content and temperature are low (Peacock and Hyndman,

446 1999). Talc was not widely observed in the paleo-mantle wedge exposed in the Shiraga body, central

447   Shikoku, Japan, at the temperature–pressure condition where the antigorite–brucite system is

448   thermodynamically stable (Kawahara et al., 2016; Mizukami et al., 2014). Although only the antigorite

449   exists stably in the antigorite–brucite stability field when the Si content is high, brucite is widely distributed

450   in the Shiraga body (~10–15 %), suggesting low Si metasomatism in the shallow hydrated mantle wedge

451   (Kawahara et al., 2016). Hence, brucite can stably exist within the mantle wedge rather than talc. Although

452   talc is still significantly important for the deformation at the subduction plate interface (Hirauchi et al.,

453   2013), the possible occurrence of brucite and its weak and unstable frictional characteristics implies that

454   brucite may be a possible control for the seismic activities at the subduction plate interface in the shallow

455   hydrated mantle wedge.

456   The results of recent seismological studies showed that plate interfaces in the shallow mantle

457   wedge have a nearly lithostatic pore pressure due to slab-derived water at various subduction zones such as

458   SE Japan, Cascadia, Central Mexico, and Hikurangi (Audet et al., 2009; Audet and Kim, 2016; Eberhart-

459   Phillips and Reyners, 2012; Matsubara et al., 2009; Shelly et al., 2006; Song and Kim, 2012). Such low

460   effective normal stress conditions are conducive for brittle deformation rather than ductile behavior (French

461   and Condit, 2019; Gao and Wang, 2017). Slow earthquakes in the mantle wedge of various subduction

462   zones (Audet and Kim, 2016; Obara and Kato, 2016) might be induced by the low effective normal stress

463   because the low effective normal stress conditions are conducive for the nucleation of slow earthquakes

464   (Liu and Rice, 2007, 2009; Rubin, 2008; Segall et al., 2010). As the $a - b$ value of brucite decreases with

465   decreasing effective normal stress, brucite at low effective normal stress possibly causes the nucleation of

466   slow earthquakes in the mantle wedge. On the other hand, an increase in $a - b$ value at higher stresses

467   was caused by the decrease in b value (see section 3.1.2), which may be related to the saturation of the

468   real area of contact (Saffer and Marone, 2003). As the b value can be recast as the healing rate in slide-

469   hold-slide type experiments (Ikari et al., 2016), wet brucite cannot store strain energy at the high effective

470   normal stress condition. Notably, the possible presence of talc or brucite-free antigorite due to high Si

471   content in the vicinity of the slab–mantle interface (Hirauchi et al., 2013; Peacock and Hyndman, 1999)

472   might affect the partitioning of deformation (French and Condit, 2019) and the contribution of brucite to

473   the deformation. The mechanisms of nucleation of slow earthquakes are still debated from both theoretical

474   and experimental studies, for example, the dilatancy hardening, the transition from negative to positive $a -$

475   b value, the slip-weakening, or the slow stick-slip are all considered possible mechanisms (den Hartog et

476   al., 2012; Ikari et al., 2013; Leeman et al., 2016, 2018; Matsuzawa et al., 2010; Okazaki and Katayama,

477   2015; Rubin, 2008; Segall et al., 2010; Shibazaki and Iio, 2003). As other serpentinite-related minerals

478   show stable frictional behavior, i.e., positive $a - b$, friction experiments with mixtures of brucite and other

479   minerals like talc or antigorite may provide further information on the generation of slow earthquakes. In

480   addition, the linkage between high pore fluid pressure and the effective normal stress is still debated (Hirth

481   and Beeler, 2015; Noda and Takahashi, 2016); therefore, experiments under hydrothermal conditions with

482   high confining pressure and high pore fluid pressure must be conducted in the future.

483

484

485
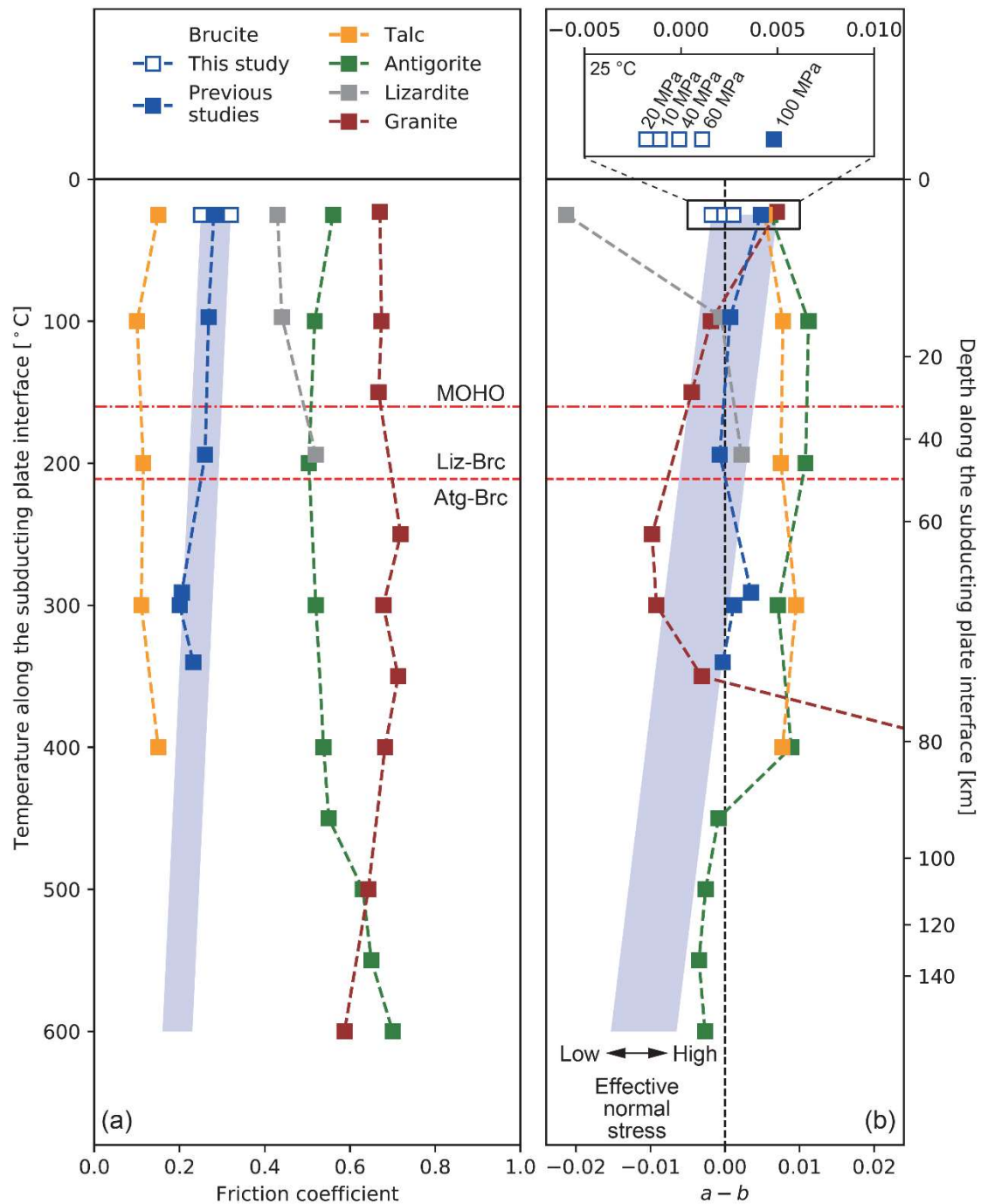
Figure 8: Friction coefficients (a) and velocity dependences (b) of brucite (this study; Moore et al., 2001), talc (Moore and Lockner, 2008), antigorite (Okazaki and Katayama, 2015; Takahashi et al., 2011), lizardite (Moore et al., 1997), and granite (Blanpied et al., 1998). The vertical axes are identical to the temperature gradient along the subduction plate interface in NE Japan (Peacock and Wang, 1999). The red chain horizontal line represents the typical depth of the MOHO. The red dotted horizontal line represents the phase boundary between lizardite– brucite (Liz–Brc) and antigorite–brucite (Atg–Brc; Peacock and Hyndman, 1999). The blue shaded areas are

the estimated frictional characteristics extrapolated from experimental results. With the decrease in the effective

normal stress, the $a - b$ value decreases, as indicated by the arrow. This trend was confirmed at room

temperature, as shown in the inset at the top of (b) and Fig. 4.

5. Conclusions

In this study, the influence of effective normal stress on the frictional characteristics of brucite

was experimentally determined under both dry and wet conditions at room temperature. The final friction

coefficients of brucite are 0.40 and 0.26 in the dry and wet cases, respectively, independently of the applied

normal stress, while the peak friction coefficients are inversely correlated with the applied normal stress.

In all dry experiments, velocity-weakening or stick-slip behavior was observed at every normal stress. In

the wet experiments, velocity-weakening, -neutral, and -strengthening behaviors were observed at normal

stresses of 10 and 20, 40, and 60 MPa, respectively. Combining with the previously reported temperature

effect, this result suggests that brucite is weak and unstable under a wide range of temperature–pressure

conditions. The microstructural observations reveal that the low friction coefficient and slip weakening

from the peak to steady-state friction coefficient are due to the smooth boundary shear and basal plane

orientation parallel to the boundary shear. Because the deformation is concentrated within a narrow shear

band with a thickness less than 50 μm, a small amount of brucite can weaken the bulk strength of the

antigorite–brucite assemblage. Compared to other serpentinite minerals, brucite is the only mineral that

shows both low friction coefficient and velocity-weakening behavior. Hence, we conclude that weak,

unstable brucite contributes to the nucleation of slow earthquakes in the shallow hydrated mantle wedge.

Table 1. *Summary of the experimental conditions and results.*

	Friction coefficient	$a - b$

Experiment	Condition	Normal stress	Final shear displacement	Peak value	Steady state (10 mm)	Steady state (20 mm)	Upsteps[a]	Downsteps[a]
HTB550	Dry	20 MPa	18 mm	0.67	0.36	0.35[b]	N/A	N/A
HTB575	Dry	20 MPa	20 mm	0.68	0.46	0.44	-0.0047±0.0003	-0.0048±0.0002
HTB580	Dry	10 MPa	20 mm	0.77	0.49	0.45	-0.0024±0.0004	-0.0014±0.0003
ND1	Dry	20 MPa	0 mm	N/A	N/A	N/A	N/A	N/A
HTB593	Dry	20 MPa	1.5 mm[c]	N/A	N/A	N/A	N/A	N/A
HTB595	Dry	20 MPa	2.0 mm[d]	0.60	N/A	N/A	N/A	N/A
HTB598	Dry	20 MPa	20 mm	0.61	0.41	0.39	-0.0010±0.0002	-0.0009±0.0002
HTB601	Dry	20 MPa	10 mm	0.65	0.42	N/A	N/A	N/A
HTB641	Dry	40 MPa	20 mm	0.51	0.41	0.395	-0.0031±0.0003[e]	-0.0020±0.0004[e]
HTB642	Dry	60 MPa	20 mm	0.50	0.40	0.39	-0.0034±0.0008[e]	-0.0012±0.0006[e]
HTB734	Wet	20 MPa	20 mm	0.35	0.28	0.25	-0.0011±0.0002	-0.0018±0.0001
HTB735	Wet	20 MPa	10 mm	0.37	0.29	N/A	N/A	N/A

HTB736	Wet	20 MPa	1.2 mm[c]	N/A	N/A	N/A	N/A	N/A
HTB737	Wet	10 MPa	20 mm	0.39	0.32	0.31	-0.0010±0.0003	-0.0011±0.0002
HTB738	Wet	20 MPa	1.8 mm[d]	0.34	N/A	N/A	N/A	N/A
HTB739	Wet	40 MPa	20 mm	0.29	0.26	0.24	0.0001±0.0002	-0.0001±0.0001
HTB741	Wet	60 MPa	20 mm	0.33	0.25	0.25	0.0012±0.0001	0.0011±0.0001

Note. [a]All parameters (a, b, and d_c) used for the velocity step tests are listed in Table S1. [b]Value at a shear displacement of 18 mm. [c]Shear loading was stopped before the peak friction coefficient was reached. [d]Shear loading was stopped shortly after the peak friction coefficient was reached. [e]Stick-slip behavior was observed and $a - b$ value was determined by eq. 5.

514

Data availability

516   The results of all experimental data are available in the Supporting Information.

517

Author contributions

519   H.O. conceptualized this study. H.O. and I.K. conducted the experiments. H.O. and H.S.

520 conducted analyses before experiments. H.O. carried out formal analyses and microstructural analyses. H.O.

521 prepared the original manuscript, which was reviewed and edited by all coauthors. K.K. was the supervisor.

522 I.K., H.S., and K.K. designed the research project.

523

524 **Competing interests**

525 The authors declare that they have no conflict of interest.

526

527 **Acknowledgement**

528 We thank two anonymous referees for their careful and constructive reviews. We also thank Y.

529 Noda and R. Fujioka for the experiments, H. Ishisako for the preparation of thin sections, and A. Yamaguchi

530 and N. Ogawa for SEM observations. This research was supported by KAKENHI grants (JP20J20413,

531 JP20H00200, JP15H02147), and the Cooperative Program (No. 114, 2019) of the Atmosphere and Ocean

532 Research Institute, University of Tokyo. H.O. is supported by JSPS and FMSP as a research fellow.

533

534 **References**

535 Angiboust, S. and Agard, P.: Initial water budget: The key to detaching large volumes of eclogitized

536 oceanic crust along the subduction channel?, Lithos, 120, 453–474, doi:10.1016/j.lithos.2010.09.007,

537 2010.

538 Anthony, J. L. and Marone, C.: Influence of particle characteristics on granular friction, J. Geophys. Res.,

539 110, B08409, doi:10.1029/2004JB003399, 2005.

540 Audet, P. and Kim, Y.: Teleseismic constraints on the geological environment of deep episodic slow

541 earthquakes in subduction zone forearcs: A review, Tectonophysics, 670, 1–15,

542 doi:10.1016/j.tecto.2016.01.005, 2016.

543 Audet, P., Bostock, M. G., Christensen, N. I. and Peacock, S. M.: Seismic evidence for overpressured

544 subducted oceanic crust and megathrust fault sealing, Nature, 457, 76–78, doi:10.1038/nature07650,

545 2009.

546   Berman, H.: Fibrous Brucite from Quebec, American Mineralogist, 17, 313–316, 1932.

547   Bhattacharya, P., Rubin, A. M., Bayart, E., Savage, H. M. and Marone, C.: Critical evaluation of state

548   evolution laws in rate and state friction: Fitting large velocity steps in simulated fault gouge with time-,

549   slip-, and stress-dependent constitutive laws, J. Geophys. Res. Solid Earth, 120, 6365–6385,

550   doi:10.1002/2015JB012437, 2015.

551   Bhattacharya, P., Rubin, A. M. and Beeler, N. M.: Does fault strengthening in laboratory rock friction

552   experiments really depend primarily upon time and not slip?, J. Geophys. Res. Solid Earth, 122, 6389–

553   6430, doi:10.1002/2017JB013936, 2017.

554   Blanpied, M. L., Marone, C. J., Lockner, D. A., Byerlee, J. D. and King, D. P.: Quantitative measure of

555   the variation in fault rheology due to fluid-rock interactions, J. Geophys. Res. Solid Earth, 103, 9691–

556   9712, doi:10.1029/98JB00162, 1998.

557   Bostock, M. G., Hyndman, R. D., Rondenay, S. and Peacock, S. M.: An inverted continental Moho and

558   serpentinization of the forearc mantle, Nature, 417, 536–538, doi:10.1038/417536a, 2002.

559   Calvert, A. J., Bostock, M. G., Savard, G. and Unsworth, M. J.: Cascadia low frequency earthquakes at

560   the base of an overpressured subduction shear zone, Nat. Comm., 11, 3874, doi:10.1038/s41467-020-

561   17609-3, 2020.

562   Christensen, N. I.: Serpentinites, Peridotites, and Seismology, Int. Geol. Rev., 46, 795–816,

563   doi:10.2747/0020-6814.46.9.795, 2004.

564   Collettini, C., Viti, C., Smith, S. A. F. and Holdsworth, R. E.: Development of interconnected talc

565   networks and weakening of continental low-angle normal faults, Geology, 37, 567–570,

566   doi:10.1130/G25645A.1, 2009.

567   D'Antonio, M. and Kristensen, M. B.: Serpentine and brucite of ultramafic clasts from the South

568   Chamorro Seamount (Ocean Drilling Program Leg 195, Site 1200): inferences for the serpentinization of

569   the Mariana forearc mantle, Mineral. Mag., 68, 887–904, doi:10.1180/0026461046860229, 2004.

570 Deer, W. A., Howie, R. A. and Zussman, J.: An Introduction to the Rock-Forming Minerals, 3rd edition,

571 The Mineralogical Society, London, United Kingdom, 2013.

572 den Hartog, S. A. M. and Spiers, C. J.: A microphysical model for fault gouge friction applied to

573 subduction megathrusts, J. Geophys. Res. Solid Earth, 119(2), 1510–1529, doi:10.1002/2013JB010580,

574 2014.

575 den Hartog, S. A. M., Peach, C. J., de Winter, D. A. M., Spiers, C. J. and Shimamoto, T.: Frictional

576 properties of megathrust fault gouges at low sliding velocities: New data on effects of normal stress and

577 temperature, J. Struct. Geol., 38, 156–171, doi:10.1016/j.jsg.2011.12.001, 2012.

578 DeShon, H. R. and Schwartz, S. Y.: Evidence for serpentinization of the forearc mantle wedge along the

579 Nicoya Peninsula, Costa Rica, Geophys. Res. Lett., 31, L21611, doi:10.1029/2004GL021179, 2004.

580 Dieterich, J. H.: Modeling of rock friction: 1. Experimental results and constitutive equations, J. Geophys.

581 Res., 84, 2161, doi:10.1029/JB084iB05p02161, 1979.

582 Dorbath, C., Gerbault, M., Carlier, G. and Guiraud, M.: Double seismic zone of the Nazca plate in

583 northern Chile: High-resolution velocity structure, petrological implications, and thermomechanical

584 modeling, Geochem. Geophys. Geosyst., 9, Q07006, doi:10.1029/2008GC002020, 2008.

585 Eberhart-Phillips, D. and Reyners, M.: Imaging the Hikurangi Plate interface region, with improved local-

586 earthquake tomography, Geophys. J. Int., 190, 1221–1242, doi:10.1111/j.1365-246X.2012.05553.x, 2012.

587 Evans, B. W., Hattori, K. and Baronnet, A.: Serpentinite: What, Why, Where?, Elements, 9, 99–106,

588 doi:10.2113/gselements.9.2.99, 2013.

589 Fagereng, Å. and den Hartog, S. A. M.: Subduction megathrust creep governed by pressure solution and

590 frictional–viscous flow, Nat. Geosci., 10, 51–57, doi:10.1038/ngeo2857, 2017.

591 French, M. E. and Condit, C. B.: Slip partitioning along an idealized subduction plate boundary at deep

592 slow slip conditions, Earth Planet. Sci. Lett., 528, 115828, doi:10.1016/j.epsl.2019.115828, 2019.

593   Gao, X. and Wang, K.: Rheological separation of the megathrust seismogenic zone and episodic tremor

594   and slip, Nature, 543, 416–419, doi:10.1038/nature21389, 2017.

595   Giorgetti, C., Carpenter, B. M. and Collettini, C.: Frictional behavior of talc-calcite mixtures, J. Geophys.

596   Res. Solid Earth, 120, 6614–6633, doi:10.1002/2015JB011970, 2015.

597   Guillot, S. and Hattori, K.: Serpentinites: Essential roles in geodynamics, arc volcanism, sustainabled, and

598   the origin of life, Elements, 9, 95–98, doi:10.2113/gselements.9.2.95, 2013.

599   Guillot, S., Hattori, K., Agard, P., Schwartz, S. and Vidal, O.: Exhumation processes in oceanic and

600   continental subduction conetxts: a review, in: Subduction zone geodynamics, edited by S. Lallemand and

601   F. Funiciello, Springer, Berlin, Heidelberg, Germany, 175–205, 2009.

602   Guillot, S., Schwartz, S., Reynard, B., Agard, P. and Prigent, C.: Tectonic significance of serpentinites,

603   Tectonophysics, 646, 1–19, doi:10.1016/j.tecto.2015.01.020, 2015.

604   Haines, S. H., Kaproth, B., Marone, C., Saffer, D. M. and van der Pluijm, B. A.: Shear zones in clay-rich

605   fault gouge: A laboratory study of fabric development and evolution, J. Struct. Geol., 51, 206–225,

606   doi:10.1016/j.jsg.2013.01.002, 2013.

607   Hirauchi, K., den Hartog, S. A. M. and Spiers, C. J.: Weakening of the slab–mantle wedge interface

608   induced by metasomatic growth of talc, Geology, 41, 75–78, doi:10.1130/G33552.1, 2013.

609   Hirth, G. and Beeler, N. M.: The role of fluid pressure on frictional behavior at the base of the

610   seismogenic zone, Geology, 43, 223–226, doi:10.1130/G36361.1, 2015.

611   Hirth, G. and Guillot, S.: Rheology and tectonic significance of serpentinite, Elements, 9, 107–113,

612   doi:10.2113/gselements.9.2.107, 2013.

613   Horn, H. M. and Deere, D. U.: Frictional characteristics of minerals, Géotechnique, 12, 319–335,

614   doi:10.1680/geot.1962.12.4.319, 1962.

615   Hostetler, P. B., Coleman, R. G., Mumpton, F. A. and Evans, B. W.: Brucite in Alpine Serpentinites, Am.

616   Mineralogist, 51, 75–98, 1966.

617   Hyndman, R. D. and Peacock, S. M.: Serpentinization of the forearc mantle, Earth Planet. Sci. Lett., 212,

618   417–432, doi:10.1016/S0012-821X(03)00263-2, 2003.

619   Ide, S., Beroza, G. C., Shelly, D. R. and Uchide, T.: A scaling law for slow earthquakes, Nature, 447, 76–

620   79, doi:10.1038/nature05780, 2007.

621   Ikari, M. J., Marone, C., Saffer, D. M. and Kopf, A. J.: Slip weakening as a mechanism for slow

622   earthquakes, Nat. Geosci., 6, 468–472, doi:10.1038/ngeo1818, 2013.

623   Ikari, M. J., Carpenter, B. M. and Marone, C.: A microphysical interpretation of rate- and state-dependent

624   friction for fault gouge, Geochem. Geophys. Geosyst., 17, 1660–1677, doi:10.1002/2016GC006286,

625   2016.

626   Kawahara, H., Endo, S., Wallis, S. R., Nagaya, T., Mori, H. and Asahara, Y.: Brucite as an important

627   phase of the shallow mantle wedge: Evidence from the Shiraga unit of the Sanbagawa subduction zone,

628   SW Japan, Lithos, 254–255, 53–66, doi:10.1016/j.lithos.2016.02.022, 2016.

629   Kawai, K., Sakuma, H., Katayama, I. and Tamura, K.: Frictional characteristics of single and

630   polycrystalline muscovite and influence of fluid chemistry, J. Geophys. Res. Solid Earth, 120, 6209–

631   6218, doi:10.1002/2015JB012286, 2015.

632   Kawakatsu, H. and Watada, S.: Seismic evidence for deep-water transportation in the mantle, Science,

633   316, 1468–1471, doi:10.1126/science.1140855, 2007.

634   Kenigsberg, A. R., Rivière, J., Marone, C. and Saffer, D. M.: The effects of shear strain, fabric, and

635   porosity evolution on elastic and mechanical properties of clay-rich fault gouge, J. Geophys. Res. Solid

636   Earth, 10968-10982, doi:10.1029/2019JB017944, 2019.

637   Kenigsberg, A. R., Rivière, J., Marone, C. and Saffer, D. M.: Evolution of Elastic and Mechanical

638   Properties During Fault Shear: The Roles of Clay Content, Fabric Development, and Porosity, J.

639   Geophys. Res. Solid Earth, 125, e2019JB018612, doi:10.1029/2019JB018612, 2020.

640   Leeman, J. R., Saffer, D. M., Scuderi, M. M. and Marone, C.: Laboratory observations of slow

641   earthquakes and the spectrum of tectonic fault slip modes, Nat. Comm., 7, 11104,

642   doi:10.1038/ncomms11104, 2016.

643   Leeman, J. R., Marone, C. and Saffer, D. M.: Frictional mechanics of slow earthquakes, J. Geophys. Res.

644   Solid Earth, 123, 7931–7949, doi:10.1029/2018JB015768, 2018.

645   Liu, Y. and Rice, J. R.: Spontaneous and triggered aseismic deformation transients in a subduction fault

646   model, J. Geophys. Res., 112, B09404, doi:10.1029/2007JB004930, 2007.

647   Liu, Y. and Rice, J. R.: Slow slip predictions based on granite and gabbro friction data compared to GPS

648   measurements in northern Cascadia, J. Geophys. Res. Solid Earth, 114, 1–19,

649   doi:10.1029/2008JB006142, 2009.

650   Logan, J. M. and Rauenzahn, K. A.: Frictional dependence of gouge mixtures of quartz and

651   montmorillonite on velocity, composition and fabric, Tectonophysics, 144, 87–108, doi:10.1016/0040-

652   1951(87)90010-2, 1987.

653   Logan, J. M., Dengo, C. A., Higgs, N. G. and Wang, Z. Z.: Fabrics of experimental fault zones: Their

654   development and eelationship to mechanical behavior, in: Fault Mechanics and Transport Properties of

655   Rocks, edited by Evans, B, and Wong, T.F., Elsevier, 33–67, 1992.

656   Manning, C. E.: Coupled reaction and flow in subduction zones: Silica metasomatism in the mantle

657   wedge, in Fluid Flow and Transport in Rocks, edited by Jamtveit, B., and Yardley, B.W.D., Springer,

658   Dordrecht, the Netherlands, 139-148, 1997.

659   Marone, C.: Laboratory-derived friction laws and their application to seismic faulting, Annu. Rev. Earth

660   Planet. Sci., 26, 643–696, doi:10.1146/annurev.earth.26.1.643, 1998.

661   Marone, C. and Kilgore, B. D.: Scaling of the critical slip distance for seismic faulting with shear strain in

662   fault zones, Nature, 362, 618–621, doi:10.1038/362618a0, 1993.

663   Matsubara, M., Obara, K. and Kasahara, K.: High-VP/VS zone accompanying non-volcanic tremors and

664   slow-slip events beneath southwestern Japan, Tectonophysics, 472, 6–17,

665   doi:10.1016/j.tecto.2008.06.013, 2009.

666   Matsuzawa, T., Hirose, H., Shibazaki, B. and Obara, K.: Modeling short- and long-term slow slip events

667   in the seismic cycles of large subduction earthquakes, J. Geophys. Res., 115, B12301,

668   doi:10.1029/2010JB007566, 2010.

669   Mizukami, T., Yokoyama, H., Hiramatsu, Y., Arai, S., Kawahara, H., Nagaya, T. and Wallis, S. R.: Two

670   types of antigorite serpentinite controlling heterogeneous slow-slip behaviours of slab–mantle interface,

671   Earth Planet. Sci. Lett., 401, 148–158, doi:10.1016/j.epsl.2014.06.009, 2014.

672   Moore, D. E. and Lockner, D. A.: Crystallographic controls on the frictional behavior of dry and water-

673   saturated sheet structure minerals, J. Geophys. Res., 109, B03401, doi:10.1029/2003JB002582, 2004.

674   Moore, D. E. and Lockner, D. A.: Comparative deformation behavior of minerals in serpentinized

675   ultramafic rock: Application to the slab-mantle interface in subduction zones, Int. Geol. Rev., 49, 401–

676   415, doi:10.2747/0020-6814.49.5.401, 2007.

677   Moore, D. E. and Lockner, D. A.: Talc friction in the temperature range 25°–400 °C: Relevance for Fault-

678   Zone Weakening, Tectonophysics, 449, 120–132, doi:10.1016/j.tecto.2007.11.039, 2008.

679   Moore, D. E. and Lockner, D. A.: Frictional strengths of talc-serpentine and talc-quartz mixtures, J.

680   Geophys. Res., 116, B01403, doi:10.1029/2010JB007881, 2011.

681   Moore, D. E., Lockner, D. A., Ma, S., Summers, R. and Byerlee, J. D.: Strengths of serpentinite gouges at

682   elevated temperatures, J. Geophys. Res. Solid Earth, 102, 14787–14801, doi:10.1029/97JB00995, 1997.

683   Moore, D. E., Lockner, D. A., Iwata, K., Tanaka, H. and Byerlee, J. D.: How brucite may affect the

684   frictional properties of serpentinite, USGS Open-File Report, 1–14, 2001.

685   Morrow, C. A., Moore, D. E. and Lockner, D. A.: The effect of mineral bond strength and adsorbed water

686   on fault gouge frictional strength, Geophys. Res. Lett., 27, 815–818, doi:10.1029/1999GL008401, 2000.

687   Nagaya, T., Okamoto, A., Oyanagi, R., Seto, Y., Miyake, A., Uno, M., Muto, J. and Wallis, S. R.:

688   Crystallographic preferred orientation of talc determined by an improved EBSD procedure for sheet

689   silicates: Implications for anisotropy at the slab–mantle interface due to Si-metasomatism, Am.

690   Mineralogist, 105, 873–893, doi:10.2138/am-2020-7006, 2020.

691   Nakajima, J., Tsuji, Y., Hasegawa, A., Kita, S., Okada, T. and Matsuzawa, T.: Tomographic imaging of

692   hydrated crust and mantle in the subducting Pacific slab beneath Hokkaido, Japan: Evidence for

693   dehydration embrittlement as a cause of intraslab earthquakes, Gondwana Res., 16, 470–481,

694   doi:10.1016/j.gr.2008.12.010, 2009.

695   Niemeijer, A. R.: Velocity-dependent slip weakening by the combined operation of pressure solution and

696   foliation development, Sci. Rep., 8, 4724, doi:10.1038/s41598-018-22889-3, 2018.

697   Niemeijer, A. R. and Spiers, C. J.: A microphysical model for strong velocity weakening in phyllosilicate-

698   bearing fault gouges, J. Geophys. Res., 112, B10405, doi:10.1029/2007JB005008, 2007.

699   Noda, H. and Shimamoto, T.: Constitutive properties of clayey fault gouge from the Hanaore fault zone,

700   southwest Japan, J. Geophys. Res., 114, B04409, doi:10.1029/2008JB005683, 2009.

701   Noda, H. and Takahashi, M.: The effective stress law at a brittle-plastic transition with a halite gouge

702   layer, Geophys. Res. Lett., 43, 1966–1972, doi:10.1002/2015GL067544, 2016.

703   Obara, K.: Nonvolcanic Deep Tremor Associated with Subduction in Southwest Japan, Science, 296,

704   1679–1681, doi:10.1126/science.1070378, 2002.

705   Obara, K. and Kato, A.: Connecting slow earthquakes to huge earthquakes, Science, 353, 253–257,

706   doi:10.1126/science.aaf1512, 2016.

707   Okamoto, A. S., Verberne, B. A., Niemeijer, A. R., Takahashi, M., Shimizu, I., Ueda, T. and Spiers, C. J.:

708   Frictional properties of simulated chlorite gouge at hydrothermal conditions: Implications for subduction

709   megathrusts, J. Geophys. Res. Solid Earth, 124, 4545–4565, doi:10.1029/2018JB017205, 2019.

710   Okazaki, K. and Katayama, I.: Slow stick slip of antigorite serpentinite under hydrothermal conditions as

711   a possible mechanism for slow earthquakes, Geophys. Res. Lett., 42, 1099–1104,

712   doi:10.1002/2014GL062735, 2015.

713   Okuda, H., Kawai, K. and Sakuma, H.: First-principles investigation of frictional characteristics of

714   brucite: An application to its macroscopic frictional characteristics, J. Geophys. Res. Solid Earth, 124,

715   10423–10443, doi:10.1029/2019JB017740, 2019.

716   Oleskevich, D. A., Hyndman, R. D. and Wang, K.: The updip and downdip limits to great subduction

717   earthquakes: Thermal and structural models of Cascadia, south Alaska, SW Japan, and Chile, J. Geophys.

718   Res. Solid Earth, 104, 14965–14991, doi:10.1029/1999JB900060, 1999.

719   Oyanagi, R., Okamoto, A., Hirano, N. and Tsuchiya, N.: Competitive hydration and dehydration at

720   olivine–quartz boundary revealed by hydrothermal experiments: Implications for silica metasomatism at

721   the crust–mantle boundary, Earth Planet. Sci. Lett., 425, 44–54, doi:10.1016/j.epsl.2015.05.046, 2015.

722   Oyanagi, R., Okamoto, A. and Tsuchiya, N.: Silica controls on hydration kinetics during serpentinization

723   of olivine: Insights from hydrothermal experiments and a reactive transport model, Geochim.

724   Cosmochim. Acta, 270, 21–42, doi:10.1016/j.gca.2019.11.017, 2020.

725   Peacock, S. M. and Hyndman, R. D.: Hydrous minerals in the mantle wedge and the maximum depth of

726   subduction thrust earthquakes, Geophys. Res. Lett., 26, 2517–2520, doi:10.1029/1999GL900558, 1999.

727   Peacock, S. M. and Wang, K.: Seismic consequences of warm versus cool subduction metamorphism:

728   Examples from southwest and northeast Japan, Science, 286, 937–939,

729   doi:10.1126/science.286.5441.937, 1999.

730   Ramachandran, K. and Hyndman, R. D.: The fate of fluids released from subducting slab in northern

731   Cascadia, Solid Earth, 3, 121–129, doi:10.5194/se-3-121-2012, 2012.

732   Reinen, L. A., Weeks, J. D. and Tullis, T. E.: The frictional behavior of lizardite and antigorite

733   serpentinites: Experiments, constitutive models, and implications for natural faults, Pure Applied

734   Geophys., 143, 317–358, doi:10.1007/BF00874334, 1994.

735   Reynard, B.: Serpentine in active subduction zones, Lithos, 178, 171–185,

736   doi:10.1016/j.lithos.2012.10.012, 2013.

737   Rogers, G. and Dragert, H.: Episodic tremor and slip on the Cascadia subduction zone: The chatter of

738   silent slip, Science, 300, 1942–1943, doi:10.1126/science.1084783, 2003.

739   Rubin, A. M.: Episodic slow slip events and rate-and-state friction, J. Geophys. Res., 113, B11414,

740   doi:10.1029/2008JB005642, 2008.

741   Rubinstein, J. L., Vidale, J. E., Gomberg, J., Bodin, P., Creager, K. C. and Malone, S. D.: Non-volcanic

742   tremor driven by large transient shear stresses, Nature, 448, 579–582, doi:10.1038/nature06017, 2007.

743   Rubinstein, J. L., La Rocca, M., Vidale, J. E., Creager, K. C. and Wech, A. G.: Tidal Modulation of

744   Nonvolcanic Tremor, Science, 319, 186–189, doi:10.1126/science.1150558, 2008.

745   Ruina, A. L.: Slip instability and state variable friction laws, J. Geophys. Res. Solid Earth, 88, 10359–

746   10370, doi:10.1029/JB088iB12p10359, 1983.

747   Saffer, D. M. and Marone, C.: Comparison of smectite- and illite-rich gouge frictional properties:

748   application to the updip limit of the seismogenic zone along subduction megathrusts, Earth Planet. Sci.

749   Lett., 215, 219–235, doi:10.1016/S0012-821X(03)00424-2, 2003.

750   Sánchez-Roa, C., Faulkner, D. R., Boulton, C., Jimenez-Millan, J. and Nieto, F.: How phyllosilicate

751   mineral structure affects fault strength in Mg-rich fault systems, Geophys. Res. Lett., 44, 5457–5467,

752   doi:10.1002/2017GL073055, 2017.

753   Schmidt, D. A. and Gao, H.: Source parameters and time-dependent slip distributions of slow slip events

754   on the Cascadia subduction zone from 1998 to 2008, J. Geophys. Res., 115, B00A18,

755   doi:10.1029/2008JB006045, 2010.

756   Segall, P., Rubin, A. M., Bradley, A. M. and Rice, J. R.: Dilatant strengthening as a mechanism for slow

757   slip events, J. Geophys. Res., 115, B12305, doi:10.1029/2010JB007449, 2010.

758   Shelly, D. R., Beroza, G. C., Ide, S. and Nakamula, S.: Low-frequency earthquakes in Shikoku, Japan,

759   and their relationship to episodic tremor and slip, Nature, 442, 188–191, doi:10.1038/nature04931, 2006.

760   Shibazaki, B. and Iio, Y.: On the physical mechanism of silent slip events along the deeper part of the

761   seismogenic zone, Geophys. Res. Lett., 30, 1489, doi:10.1029/2003GL017047, 2003.

762   Shimamoto, T. and Logan, J. M.: Effects of simulated clay gouges on the sliding behavior of Tennessee

763   sandstone, Tectonophysics, 75, 243–255, doi:10.1016/0040-1951(81)90276-6, 1981.

764   Siman-Tov, S., Aharonov, E., Sagy, A. and Emmanuel, S.: Nanograins form carbonate fault mirrors,

765   Geology, 41, 703–706, doi:10.1130/G34087.1, 2013.

766   Skarbek, R. M. and Savage, H. M.: RSFit3000: A MATLAB GUI-based program for determining rate

767   and state frictional parameters from experimental data, Geosphere, 15, 1665–1676,

768   doi:10.1130/GES02122.1, 2019.

769   Song, T.-R. A. and Kim, Y.: Localized seismic anisotropy associated with long-term slow-slip events

770   beneath southern Mexico, Geophys. Res. Lett., 39, L09308, doi:10.1029/2012GL051324, 2012.

771   Takahashi, M., Mizoguchi, K., Kitamura, K. and Masuda, K.: Effects of clay content on the frictional

772   strength and fluid transport property of faults, J. Geophys. Res., 112, B08206,

773   doi:10.1029/2006JB004678, 2007.

774   Takahashi, M., Uehara, S.-I., Mizoguchi, K., Shimizu, I., Okazaki, K. and Masuda, K.: On the transient

775   response of serpentine (antigorite) gouge to stepwise changes in slip velocity under high-temperature

776   conditions, J. Geophys. Res., 116, B10405, doi:10.1029/2010JB008062, 2011.

777   Tarling, M. S., Smith, S. A. F. and Scott, J. M.: Fluid overpressure from chemical reactions in serpentinite

778   within the source region of deep episodic tremor, Nat. Geosci., 12, 1034–1042, doi:10.1038/s41561-019-

779   0470-z, 2019.

780   Tembe, S., Lockner, D. A. and Wong, T.-F.: Effect of clay content and mineralogy on frictional sliding

781   behavior of simulated gouges: Binary and ternary mixtures of quartz, illite, and montmorillonite, J.

782   Geophys. Res., 115, B03416, doi:10.1029/2009JB006383, 2010.

783   Tesei, T., Harbord, C. W. A., De Paola, N., Collettini, C. and Viti, C.: Friction of mineralogically

784   controlled serpentinites and implications for fault weakness, J. Geophys. Res. Solid Earth, 123, 6976–

785   6991, doi:10.1029/2018JB016058, 2018.

786   Verberne, B. A., De Bresser, J. H. P., Niemeijer, A. R., Spiers, C. J., de Winter, D. A. M. and Plümper,

787   O.: Nanocrystalline slip zones in calcite fault gouge show intense crystallographic preferred orientation:

788   Crystal plasticity at sub-seismic slip rates at 18–150 °C, Geology, 41, 863–866, doi:10.1130/G34279.1,

789   2013.

790   Verberne, B. A., Spiers, C. J., Niemeijer, A. R., De Bresser, J. H. P., de Winter, D. A. M. and Plümper,

791   O.: Frictional properties and microstructure of calcite-rich fault gouges sheared at sub-seismic sliding

792   velocities, Pure Applied Geophys., 171, 2617–2640, doi:10.1007/s00024-013-0760-0, 2014a.

793   Verberne, B. A., Plümper, O., de Winter, D. A. M. and Spiers, C. J.: Superplastic nanofibrous slip zones

794   control seismogenic fault friction, Science, 346, 1342–1344, doi:10.1126/science.1259003, 2014b.

795   Viti, C.: Exploring fault rocks at the nanoscale, J. Struct. Geol., 33, 1715–1727,

796   doi:10.1016/j.jsg.2011.10.005, 2011.

797